PNAS RESEARCH ARTICLE | BIOPHYSICS AND COMPUTATIONAL BIOLOGY

The structure of a *Cryptococcus neoformans* polysaccharide motif recognized by protective antibodies: A combined NMR and MD study

Audra A. Hargett[a,1], Hugo F. Azurmendi[a,1], Conor J. Crawford[b,c,2], Maggie P. Wear[b], Stefan Oscarson[c], Arturo Casadevall[b,3], and Darón I. Freedberg[a,3]

Contributed by Arturo Casadevall; received September 11, 2023; accepted December 2, 2023; reviewed by Adam W. Barb and Neil Ravenscroft

Cryptococcus neoformans **is a fungal pathogen responsible for cryptococcosis and cryptococcal meningitis. The *C. neoformans*' capsular polysaccharide and its shed exopolysaccharide function both as key virulence factors and to protect the fungal cell from phagocytosis. Currently, a glycoconjugate of these polysaccharides is being explored as a vaccine to protect against *C. neoformans* infection. In this study, NOE and *J*-coupling values from NMR experiments were consistent with a converged structure of the synthetic decasaccharide, GXM10-Ac_3, calculated from MD simulations. GXM10-Ac_3 was designed as an extension of glucuronoxylomannan (GXM) polysaccharide motif (M2) which is common in the clinically predominant serotype A strains and is recognized by protective forms of GXM-specific monoclonal antibodies. The M2 motif is a hexasaccharide with a three-residue α-mannan backbone, modified by β-(1→2)-xyloses (Xyl) on the first two mannoses (Man) and a β-(1→2)-glucuronic acid (GlcA) on the third Man. Combined NMR and MD analyses reveal that GXM10-Ac_3 adopts an extended structure, with Xyl/GlcA branches alternating sides along the α-mannan backbone. *O*-acetyl esters also alternate sides and are grouped in pairs. MD analysis of a twelve M2-repeating unit polymer supports the notion that the GXM10-Ac_3 structure is uniformly represented throughout the polysaccharide. This derived GXM model displays high flexibility while maintaining a structural identity, yielding insights to further explore intermolecular interactions between polysaccharides, interactions with anti-GXM mAbs, and the cryptococcal polysaccharide architecture.**

cryptococcus | capsule | polysaccharide | NMR | MD simulations

Significance

This study utilized a combined NMR and MD approach to elucidate the structure of a *Cryptococcus neoformans* glucuronoxylomannan (GXM) synthetic decasaccharide (GXM10-Ac_3), recognized by protective anti-GXM mAbs. The data revealed an extended structure in which the xylose/glucuronic acid branches and pairs of 6-*O*-acetyl esters predominantly alternate sides along the α-mannan backbone. MD analysis of a GXM polysaccharide (PS) consisting of 12 repeating units predicts an extended fluctuating chain, with the decasaccharide structure uniformly represented in the solvated PS. The GXM PS exhibits high flexibility while maintaining a structural identity. These findings lay the foundation for future studies aimed at understanding GXM PS–antibody interactions.

Cryptococcus neoformans is a fungal pathogen with a worldwide distribution, that includes environmental and urban settings (1, 2), and is the causative agent of cryptococcosis and cryptococcal meningitis (3, 4). While most exposures do not lead to overt disease, *C. neoformans* can cause serious illness with a high mortality rate in immunocompromised individuals, especially in patients with HIV infection (5–7). Resistance to commonly used antifungal drugs is increasing, which creates a need for new therapeutics, e.g., vaccines (8).

C. neoformans is surrounded by a capsular polysaccharide (CPS) that is antiphagocytic and thus functions as a major virulence factor. Infection is accompanied by shedding of exopolysaccharide (EPS) which contributes to virulence by interfering with immune mechanisms (9). One major component of both CPS and EPS is the glucuronoxylomannan (GXM) polysaccharide (PS). Currently, an experimental *C. neoformans* GXM glycoconjugate vaccine is being investigated to combat this microbial infection (10). Glycoconjugates are extremely effective vaccines that reduce the incidence of infectious diseases caused by encapsulated bacteria. For example, licensed glycoconjugate vaccines utilizing the capsular PS of specific bacteria protect against *Haemophilus influenzae, Neisseria meningitidis*, and *Streptococcus pneumoniae* bacterial infections (11). We hope that a *C. neoformans* GXM PS will similarly result in a viable glycoconjugate vaccine protective against infection by this pathogen.

A GXM repeating unit (RU) consists of an α-(1→3) linked mannose (Man) triad backbone, modified by a β-(1→2) linked glucuronic acid (GlcA) branch on the 3rd Man and β-(1→2)/β-(1→4) linked xylose (Xyl) branches (12). Additionally, Man O6 can be acetylated, but the degree of *O*-acetylation is strain-specific (13, 14). Unlike bacterial capsular PS, which have a regular RU, the *C. neoformans* GXM PS is heterogeneous and is classified into six motifs, differentiated by the location and number of Xyl branches (12, 15). These motifs were first characterized by NMR of detergent-extracted, de-*O*-acetylated, ^{13}C-enriched native GXM polymer isolates. However, NMR signal degeneracy of the PS limited spectral interpretation to only the most abundant repeating motif units present in each isolate (16–22). Of the six motifs, the M2 motif, identified in Fig. 1*A*, is commonly

Reviewers: A.W.B., University of Georgia; and N.R., University of Cape Town.

The authors declare no competing interest.

[1]A.A.H and H.F.A. contributed equally to this work.

[2]Present address: Department of Biomolecular Systems, Max Planck Institute of Colloids and Interfaces, Am Mühlenberg 1, Potsdam 14476, Germany.

[3]To whom correspondence may be addressed. Email: acasade1@jhu.edu or Daron.Freedberg@fda.hhs.gov.

This article contains supporting information online at https://www.pnas.org/lookup/suppl/doi:10.1073/pnas.2315733121/-/DCSupplemental.

Published February 8, 2024.

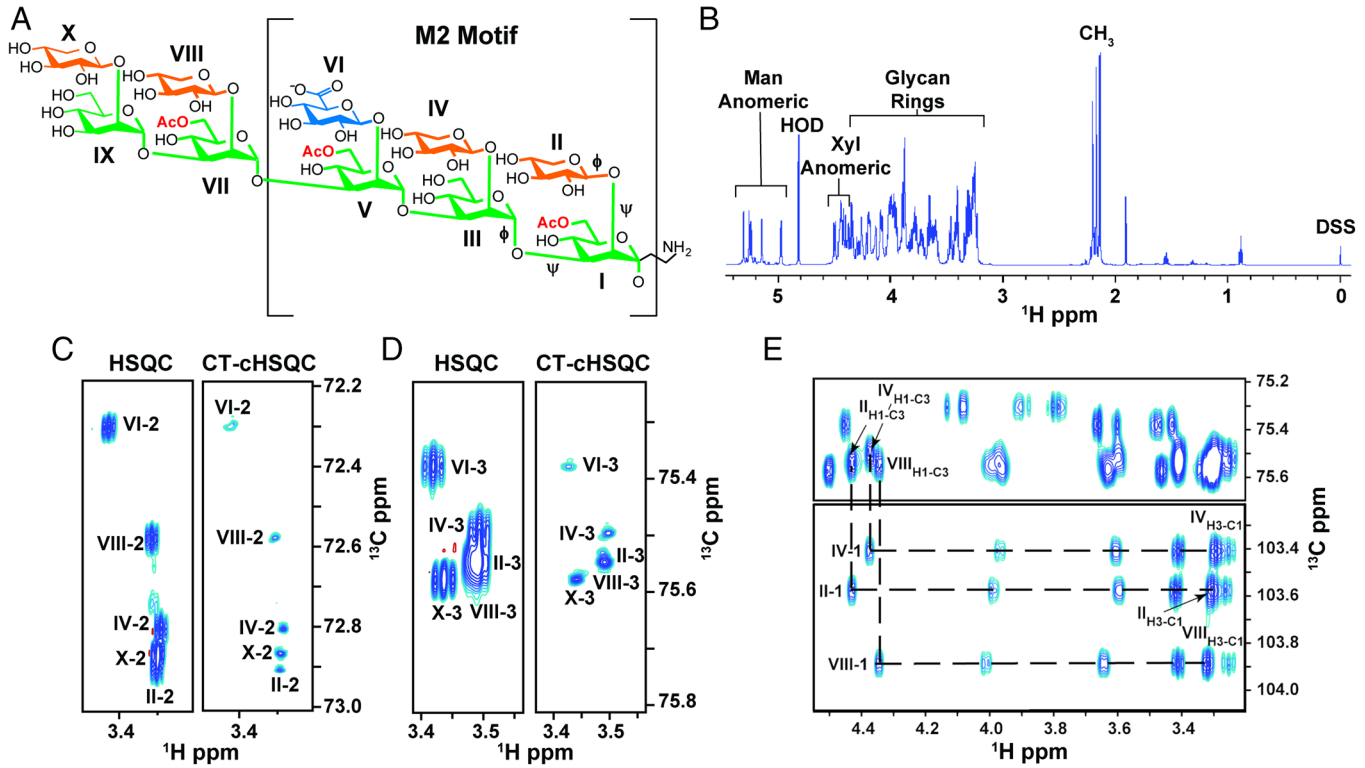

Fig. 1. *C. neoformans* GXM synthetic decasaccharide (GXM10-Ac_3) resonances are resolved through ^{1}H-^{13}C CT-cHSQC and HSQC TOCSY experiments. (*A*) GXM10-Ac_3 chemical structure contains the M2 motif, a common serotype A GXM RU, and binds strongly to anti-GXM Abs (24). Glycans are color coded as follows: Man (green), Xyl (orange), and GlcA (blue). Transglycosidic ϕ and ψ torsions are denoted on the first three residues. (*B*) GXM10-Ac_3 ^{1}H 1D identifiying diagnostic carbohydrate ^{1}H chemical shift regions. (*C* and *D*) Comparison of resolutions achieved by a standard ^{1}H-^{13}C HSQC experiment relative to a CT-cHSQC experiment, with the latter allowing assignments of previously overlapping signals in a few hours for Xyl[I, IV, X]-2 (*C*) and Xyl[II, IV, VIII]-3 (*D*). (*E*) ^{1}H-^{1}H cross-peaks between Xyl H1 and H3 obtained from a ^{1}H-^{13}C HSQC TOCSY experiment allow further differentiation between Xyl[II] and Xyl[III] H2-C2 resonances.

identified in *C. neoformans* serotype A, the most prevalent clinical form (23). The M2 motif triad is a six-residue RU consisting of a three-Man backbone with two branched β-(1→2) linked Xyl residues, followed by one β-(1→2) linked GlcA (14).

Studies utilizing GXM as an antigen have yielded mixed results. The first cryptococcal glycoconjugate vaccine, a GXM-tetanus-toxoid (GXM-TT) glycoconjugate, elicited anti-GXM antibodies and was protective in mice (25, 26). While this first glycoconjugate vaccine was not pursued further, a similar GXM-TT vaccine was later shown to elicit antibodies with the same specificity as those produced from a cryptococcal infection in a murine model (27), some of which were protective against cryptococcal infection (28). Additionally, evidence showed that *O*-acetylation is critical for binding to protective antibodies (27, 29). While cryptococcal glycoconjugate vaccines can provide protection from infection, the PS utilized in the GXM-TT vaccine is a poorly characterized, heterogeneous mixture obtained from isolating *C. neoformans* PS. One strategy to develop a chemically defined glycoconjugate vaccine is the creation of a library of synthetic GXM oligosaccharides (OSs), which are then conjugated to carrier proteins. While synthetic tetra- to heptasaccharide conjugates did not bind to protective antibodies (30), a synthetic decasaccharide (GXM10-Ac_3, Fig. 1*A*) bound strongly to several protective antibodies (24).

To better understand potential Ab–PS interactions, we characterized the three-dimensional (3D) structure of GXM10-Ac_3 by high-resolution solution NMR spectroscopy and molecular dynamics (MD) simulations and report these results herein. In this study, we alleviated the NMR signal degeneracy for GXM10-Ac_3 by using modern NMR methods and higher fields to enhance signal resolution to yield a more thorough NMR characterization. To complement the NMR data, a GXM10-Ac_3 2 μs MD simulation was conducted and found to be in general agreement with the experimental NMR data. Once an experimentally consistent GXM10-Ac_3 structure was derived, a GXM PS consisting of 12 M2 motif RUs was studied by MD to test how well the combined experimental and theoretical decasaccharide results matched the extended GXM PS. The detailed structural characterization of the GXM PS provides insights into PS structural features which are likely to be important for recognition by the host immune system to neutralize the pathogen.

Results

NMR Measurements on GXM10-Ac_3. The GXM10-Ac_3 backbone is composed of five α-(1→3) linked Man, with β-(1→2) linked Xyl substitutions, except for the third Man, which bears a β-(1→2) linked GlcA. Additionally, Man I, V, and VII are acetylated at O6 (Fig. 1*A*) (24).

To verify GXM10-Ac_3's primary structure and delineate connectivity, we collected ^{1}H 1D, ^{1}H-^{13}C heteronuclear single quantum correlation (HSQC) (31), long-range heteronuclear single quantum multiple bond correlation (LR-HSQMBC) (32), and HSQC-TOCSY (HSQC-Total correlation spectroscopy) (33, 34) NMR data at 700 MHz (^{1}H frequency), 20 °C, and pH 6.5. Regions of the GXM10-Ac_3 ^{1}H 1D data can be assigned to the Man anomeric (5.34 to 4.95 ppm), Xyl anomeric (4.53 to 4.31 ppm), glycan rings (4.49 to 3.20 ppm), and Man *O*-Ac methyls (2.25 to 2.21 ppm) ^{1}Hs (Fig. 1*B*). With the ^{1}H 1D data alone, the significant chemical shift overlap in ^{1}H within the glycan ring cannot be resolved; thus, we collected 2D ^{1}H-^{13}C HSQC spectra. The standard ^{1}H-^{13}C HSQC (*SI Appendix*, Fig. S1) with 4.25 Hz/pt resolution was insufficient to resolve the Xyl residue peaks (II, IV, VIII, and X) from each other without taking

Table 1. Measured and predicted NOEs for GXM10-Ac_3

$_1$H1-^{1}H NOE	NMR Obs.	MD (R6) [Å]	MD D_{range} [Å]
[I]H1 – [II]H1	**M**	**2.5**	**1.8 – 2.4 // 2.4 – 4.0**
[I]H1 – [II]H5A	**W**	**4.8**	**3.6 – ~6.0**
[I]H1 – [II]H5E	**W**	**5.9**	**4.8 – <6.0**
[I]H2 – [II]H1	**S**	**2.4**	**1.9 – 3.2**
[I]H2 – [III]H5	**W**	**2.5**	**1.9 – 3.5**
[I]H3 – [III]H1	**S**	**2.5**	**2.0 – 3.0**
[III]H1 – [IV]H1	**M**	**2.4**	**1.8 – 2.4 // 2.4 – 4.4**
[III]H2 – [IV]H1	**S**	**2.4**	**1.9 – 3.2**
[III]H2 – [IV]H2	**W**	**3.8**	**4.1 – 4.7**
[III]H3 – [II]H5A	**W**	**3.5**	**2.7 – 4.7**
[III]H3 – [II]H5E	**W**	**2.7**	**2.0 – 3.6** // 3.6 – <6.0
[III]H3 – [V]H1	**S**	**2.4**	**1.9 – 3.0**
[V]H1 – [IV]H1	**M**	**2.2**	**1.7 – 3.1** // 3.7 – 4.5
[V]H2 – [IV]H1	**S**	**2.5**	**2.0 – 3.5**
[V]H2 – [VII]H1	**S**	**2.3**	**1.8 – 2.9**
[VII]H1 – [VIII]H1	**S**	**2.3**	**1.7 – 3.6**
[VII]H2 – [VIII]H1	**S**	**2.5**	**1.9 – 3.5**
[VII]H2 – [IX]H3	**W**	**4.4**	**3.6 – 5.2**
[VII]H3 – [IX]H1	**S**	**2.3**	**1.9 – 2.9**
[IX]H1 – [X]H1	**M**	**2.4**	**1.7 – 2.8 // 2.8 – 4.2**
[IX]H2 – [X]H1	**S**	**2.5**	**1.9 – 3.3**

NOE signals were classified based on their intensities as S (strong); M (medium); or W (weak). H–H distance analysis from MD was done utilizing (R6) = $\langle r^{-6} \rangle^{-1/6}$. Most H–H distances clustered around a single population, but in a few cases, two populations were clearly distinguished. Cluster limits are indicated in the D_{range} column. All ranges are in bold, except minor populations (relative to the main cluster) indicated with "normal" font (two ranges in bold indicate similar populations).

data for multiple days to obtain 0.5 Hz/pt resolution. Specifically, the H2-C2 resonances in residues II, IV, and X (Fig. 1*C*, HSQC) and H3-C3 in residues II, IV, and VIII (Fig. 1*D*, HSQC) significantly overlap. We achieved full resolution of the H2-C2, H4-C4, and H5-C5 correlation peaks and improved resolution of the H3-C3 peaks by utilizing a CT-cHSQC (^{1}H constant time, ^{13}C-detected, ^{1}H-^{13}C HSQC) experiment, processed with SMILE-based linear prediction (35), in only 4 h of data collection (Fig. 1 *C* and *D* and *SI Appendix*, Fig. S2). However, as previously reported, this improved resolution comes with a reduction in sensitivity. Still, in the present study, the sensitivity in the shorter experiment was sufficient to make all assignments.

We obtained residue-specific GXM10-Ac_3 chemical shift assignments via a series of ^{1}H-^{13}C HSQC-TOCSY experiments using 30, 60, and 120 ms mixing times and confirmed them via a LR-HSQMBC experiment. *SI Appendix*, Fig. S1*A*, shows a ^{1}H-^{13}C HSQC of the GXM10-Ac_3 anomeric region. Each anomeric ^{1}H-^{13}C correlation is unique, and the ^{1}H and ^{13}C chemical shifts of each residue are isolated from the rest of the ring, providing a "handle" from which the ring assignments could be made. For example, the ^{1}H and ^{13}C chemical shifts for the anomeric H1-C1 of residue II are 4.45 ppm and 102.48 ppm, respectively. In the 120 ms mixing time HSQC-TOCSY, five ^{1}H cross-peaks (3.99, 3.59, 3.42, 3.31, and 3.27 ppm) are present at a ^{13}C chemical shift of 102.48 ppm. These ^{1}H cross-peaks correspond to all the ^{1}Hs in the Xyl[II] ring (Fig. 1*E*). Inter-residue linkage connectivity was determined via a LR-HSQBMC experiment. For example, the correlation peak at 4.19 ppm and 102.48 ppm connects the Man[I]-H2 with Xyl[II]-C1 (*SI Appendix*, Fig. S3). *SI Appendix*, Table S1, provides the ^{1}H and ^{13}C chemical shift assignments for GXM10-Ac_3.

In addition to the GXM10-Ac_3 cross-peaks, NMR spectra displayed peaks for partially de-*O*-acetylated decasaccharides. We assigned three additional decamers, each corresponding to the loss of one *O*-acetyl group at either Man[I]-C6, Man[V]-C6, or Man[VII]-C6 (*SI Appendix*, Fig. S4 and Table S2). Assignments for the partially de-*O*-acetylated decamers differed measurably from GXM10-Ac_3 only at the residue that lost *O*-acetylation and the proximal residues. These minor peaks were approximately six-fold less intense than the fully *O*-acetylated decasaccharide. Complete chemical shift assignments of GXM10-Ac_3 and its degradation products aided in the interpretation of the more complex NMR experiments used for structure determination (i.e., ^{1}H-^{1}H NOE and PIP-HSQMBC).

After assigning the chemical shifts, we used data from nuclear Overhauser effect spectroscopy (NOESY) (36) and ^{1}H-^{13}C pure in-phase HSQMBC (PIP-HSQMBC) (37) NMR experiments to help delineate the GXM10-Ac_3 3D conformations. ^{13}C-edited NOESY spectra revealed 21 inter-residue ^{1}H-^{1}H NOEs (Table 1). Of the NOEs observed, one very weak peak with a signal to noise ratio (SNR) of 5 to 1 between Man[III]H3 and Xyl[II]H5 was detected. We did not observe any inter-residue NOEs between Xyl/Xyl and Xyl/GlcA branching residues nor between non-consecutive Man residues in our experiments. NOE signal intensities were classified as strong, medium, or weak (*SI Appendix*, Fig. S5), and this information was used to correlate with predicted NOEs from MD simulations (discussed below).

^{1}H-^{13}C PIP-HSQMBC NMR experiments provided transglycosidic $^3J_{CH}$ values (*Materials and Methods*), which we substituted into parameterized Karplus relations to obtain phi (ϕ) and psi (ψ) transglycosidic torsion angles (*SI Appendix*, Table S3). The ϕ and ψ torsions derived from transglycosidic $^3J_{CH}$ values were similar for most cases, ranging from 2.5 Hz to 4.2 Hz for ϕ and 3.4 Hz to 5.5 Hz for ψ torsions. The $^3J_{CH}$ for H-C-O-C Man[I]-Man[III] and H-C-O-C Man[III]-Man[V] were undetectable using the conditions in our experiments. While each transglycosidic $^3J_{CH}$ value yields four potential torsion values, we narrowed down these possibilities to the most likely torsions by incorporating the results from MD analysis, as discussed next.

MD Simulation of GXM10-Ac_3. Previous MD results on a family of GXM and related oligomers reported that "the mannan backbone was consistently extended and relatively inflexible" (38). Our study used a different force field and a significantly extended duration of MD trajectories (500 ns in the previous study as compared to 2,200 ns in the present study), nonetheless yielding a similar result regarding the mannan backbone average torsion values (*SI Appendix*, Fig. S6). However, the dynamic behavior of the OS displayed in our present, extended study, is better described as flexible, given the range of torsion values visited through the MD trajectory. The torsion maps derived for only the penta-Man backbone and GXM10 (w/wo Ac_3) demonstrate that the duration of the MD was long enough for all potential conformations to be fully explored and that the effect of adding substituents to the backbone is, as previously reported by Kuttel et al., mainly limited to narrowing the spread of torsion angle values reachable (*SI Appendix*, Fig. S6).

To obtain the most reliable structural model of GXM10-Ac_3, we compared experimental NMR data with MD-derived results. Observed NOEs are usually indicative of hydrogen atoms located within average distances less than 5 Å; however, motion often results in reduced NOE peak intensities, making them appear to

be farther apart than they are in a model. We predicted NOE's from the MD trajectory with a cutoff of 5.0 Å (see *Materials and Methods* for details). Out of 21 experimentally detected NOEs (Table 1), 19 H-H distances calculated from the MD trajectory (90%) agree with the ^{1}H-^{1}H NOEs obtained. Table 1 contains the range of distances derived from the trajectory, which reflects the weighted NOE distance averages $(\langle r^{6}\rangle)^{-1/6}$. In most cases, a single range suffices to describe the MD-derived distances, but in five cases, two populations were clearly distinguished for which ranges are reported. These cases can explain some of the minor differences between observed and predicted NOEs. In addition, two NOE signals were weak as compared to the weighted distances, 2.5 and 2.7 Å, calculated from MD. These NOEs correspond to distances associated with Man[I] and its linked Xyl[II] to the contiguous backbone Man[III]. These discrepancies are most likely explained by a more flexible Man[I] (and its branched Xyl[II]) than predicted by MD. Overall, the excellent agreement with experimental NMR data lends support to the structures obtained from the MD. Furthermore, consistent with experiment, no NOEs between branching residues were predicted from the MD results.

Next, we analyzed the MD trajectory and plotted the low-energy regions on a (ϕ, ψ) transglycosidic torsion angle map (Fig. 2). The GXM10-Ac$_3$ Man backbone glycosidic torsions show low-energy conformations (<2 kcal/mol) for a relatively narrow distribution of ϕ torsions (±15°) and a wider distribution of ψ torsions (~±30°, Fig. 2*A*). These values indicate a limited, but still broad, range of motion for the Man backbone of the GXM10-Ac$_3$. Still broader is the Man-Xyl transglycosidic torsion angle population, with the presence of two or more local energy minima (Fig. 2*B*). Nevertheless, a single preferred low-energy region is distinguishable in all cases with populations one or two orders of magnitude larger than for alternative regions. Similarly, the Man[V]-GlcA[VI] transglycosidic torsion shows a preferred low-energy region with the addition of a distinct small secondary region centered at ~(15°, −65°) (Fig. 2*C*).

Subsequently, we compared the experimental transglycosidic $^{3}J_{CH}$'s values to the averaged torsions from MD simulations (Fig. 2*D* and *SI Appendix*, Tables S3 and S4). While *J*-couplings predicted from MD simulations are heavily influenced by higher populated regions, gross departures from experimental values would indicate problems with the simulation. Fig. 2*D* shows experimental and predicted $^{3}J_{CH}$ utilizing two recently published approaches (39, 40). Considering experimental errors of ±0.5 Hz and resulting MD SD (±1 to 2 Hz) both sets of values agree. This is important in that the MD results allow disambiguation of torsion values from experimental couplings, which are the result of conformational averaging. Moreover, predicted ϕ torsions mirror the experimental ones. For the measured ψ-associated couplings, the result is more ambiguous due to both the range of couplings obtained and the broad distribution of torsions predicted by MD. In Fig. 2 *A*–*C*, we show calculated torsion values from experimental *J*-couplings as gray bands overlayed to the energy maps. For clarity, we did not include torsion regions unlikely to contribute to the measured *J*-couplings based

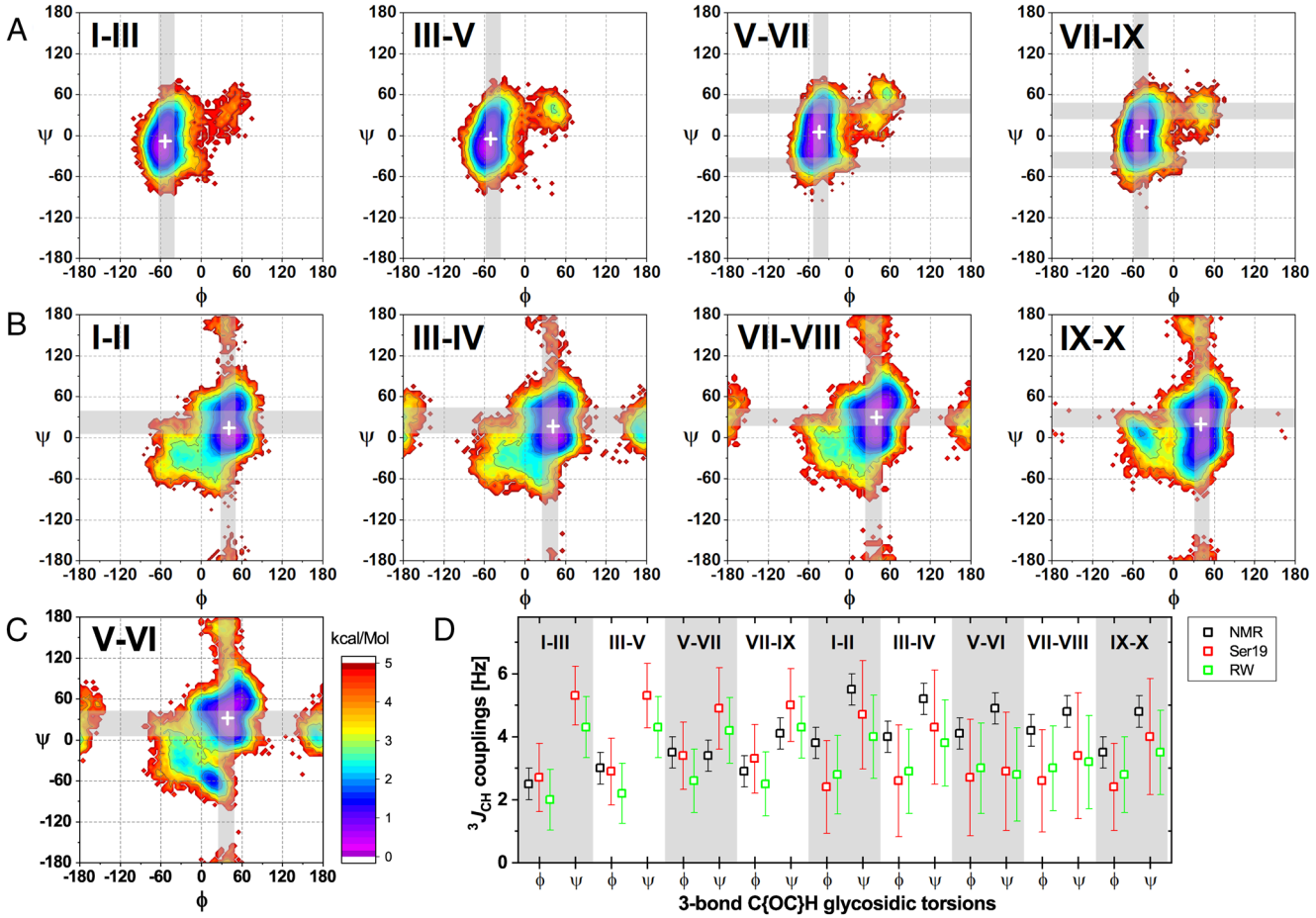

Fig. 2. GXM10-Ac$_3$ Transglycosidic torsion and $^{3}J_{CH}$-couplings analysis. (*A*–*C*) Torsion energy heatmaps generated from the MD trajectory. The most likely predicted (low-energy) conformations are denoted in purple/blue (<2 kcal/mol). Gray bands correspond to predicted torsion values from experimental $^{3}J_{CH}$ NMR values utilizing the Karplus equation as parameterized in ref. 39, which best agree with average MD trajectory torsions (white '+'). *SI Appendix*, Table S3, further details all calculated torsions. (*A*) Results for Man-Man backbone linkages. (*B*) Energy maps for Xyl-Man branched linkages. (*C*) Analysis for the GlcA-Man branch linkage. (*D*) Comparison of measured $^{3}J_{CH}$ values to MD predicted mean values using two recent approaches (*Materials and Methods*).

on the MD analysis. Importantly, Fig. 2 shows that no inconsistency is observed between the four experimentally compatible, $^3J_{CH}$-coupling derived torsion angles and the low-energy regions.

GXM10-Ac$_3$ Structural Model. We identified a representative model from the trajectory for GXM10-Ac$_3$ in solution. As a first approximation, we calculated a 2D-rmsd map of 2,200 MD frames from a 2.2 μs trajectory (hence, 1 frame/ns), selecting the 60 ring atoms of the decasaccharide (10 × 6 = 60 atoms). The map shows (*SI Appendix*, Fig. S7) that GXM10-Ac$_3$ stays in a similar shape compared to the initial conformation for about 75 ns, after which it switches to a new conformation in which it remains through the conclusion of the simulation, except for a couple of short-lived departures. Thus, we restricted the production analysis to 2 μs starting at the 100 ns mark. Taking 2,000 uniformly sampled structures (one per ns), we performed rmsd minimization on the 60 ring atoms of the first frame of the 2,000 set and obtained the resulting average structure (Fig. 3*A* and Movie S1). The resulting averaged GXM10-Ac$_3$ conforms closely to an energy-minimized structure for the backbone Mans and three of the branched Xyls [II, IV, and VII]. The GlcA[VI] and Xyl[X] averaged rings depart from the regular Xyl/GlcA pyranose chair conformation resulting in an rmsd of 0.28 and 0.31 Å, respectively. Despite the large number of calculated structures in the simulation, the computed average structure resembles an energy-minimized model. This is truly a remarkable result, as the branched glycans have ample freedom to visit a broad range of different orientations, as illustrated in Fig. 3*B*, where 500 models (sampling 500 ns of the trajectory) of the Man6Ac[V]-GlcA[VI] branch were overlayed with rmsd minimization on the six ring atoms of Man[V]. The orientation of the branch was chosen to have an unobstructed view of the β-(1→2) glycosidic linkage and the corresponding (ϕ, ψ) torsions. Two populations can be distinguished, with an approximate ratio of 95 and 5%, respectively. Naturally, the major population referred to here corresponds to the large purple/blue region in Fig. 2*C*. The acetyl group [V] is also depicted to show its almost total freedom of orientation. Movie S2 shows the dynamic behavior of GlcA for these 500 frames, utilizing the *smooth* Pymol script (with default values) for clarity. As can be inferred from the movie, the minor population is not the result of one long-persistent conformation around a local energy minimum but rather the result of multiple short-lived conformations. Similar results are obtained for all branches.

Using the averaged structure in Fig. 3*A* as a reference (referred to as GXM10ref onward), we conducted a more granular analysis calculating the rmsd against GXM10ref for models sampled every 40 ps (50,000 frames in 2 μs), which resulted in overall rmsd (60 ring atoms) of 1.6 ± 0.6 Å. The frame along the trajectory with the lowest rmsd (0.56 Å) is overlaid to GXM10ref in *SI Appendix*, Fig. S8, to provide a concrete example of how rmsd values and conformations are related. The main contributions to the rmsd value in this example can be summarized by Xyl[VIII] being misoriented by ~90° and Xyl[II, X] slightly displaced.

Thus, calculations predict, and NMR results support, the Man backbone as extended with Man-Man transglycosidic torsions fluctuating about central ϕ and ψ values. Interestingly, the average consecutive Man residues alternate orientations as result of the α-(1→3) linkage since the αC1 – O3' bond (prime indicating the next Man residue) is axial and the O3' – C3' is equatorial, and so forth (this is most easily appreciated from the left model in Fig. 3*A*). Thus, all axial bonds in contiguous Man residues are antiparallel including the substitution bonds Man[C2-O2]. Consequently, the Xyl/GlcA branches also alternate sides of the Man backbone, as shown in Fig. 3*A*. Moreover, the Man[I] and Man[V] *O*-acetyl groups are on the same side of the mannan backbone and close in space, while 6Ac[VII] is located on the opposite side. As shown in Fig. 3*B* (and accompanying Movie S2), the GlcA branch has one main population which fluctuates between two extreme orientations associated to ψ ≳ 60° (edge-on, where the plane of the ring is approximately perpendicular to the Man backbone) and ψ ≲ 20° (face-on, where the plane of the ring is parallel to the Man backbone), hence, GXM10ref in Fig. 3*A* presents an in-between orientation. *SI Appendix*, Fig. S9, shows the energy profiles through two (ϕ, ψ) torsions highlighting the low-energy barrier in the ψ dimension (~0.5 kcal/mol) leading to the spread of conformations depicted in Fig. 3*B*. The second profile (red, in *SI Appendix*, Fig. S9) is centered at the (ϕ, ψ) lowest point of the energy barrier existent to go from the lowest energy regions to conformations in the local minimum regions around (10°, –60°). This barrier can be estimated from the profile panels to be ~2.5 kcal/mol. The energy distribution displayed in Fig. 2 arises from steric interactions of the salient carboxyl group in GlcA which preferably orients the residue with the ring mostly parallel to the neighboring Xyl[II, X]. The alternative 5% minor conformation has the plane of the ring oriented perpendicular and off-line the Xyl residues.

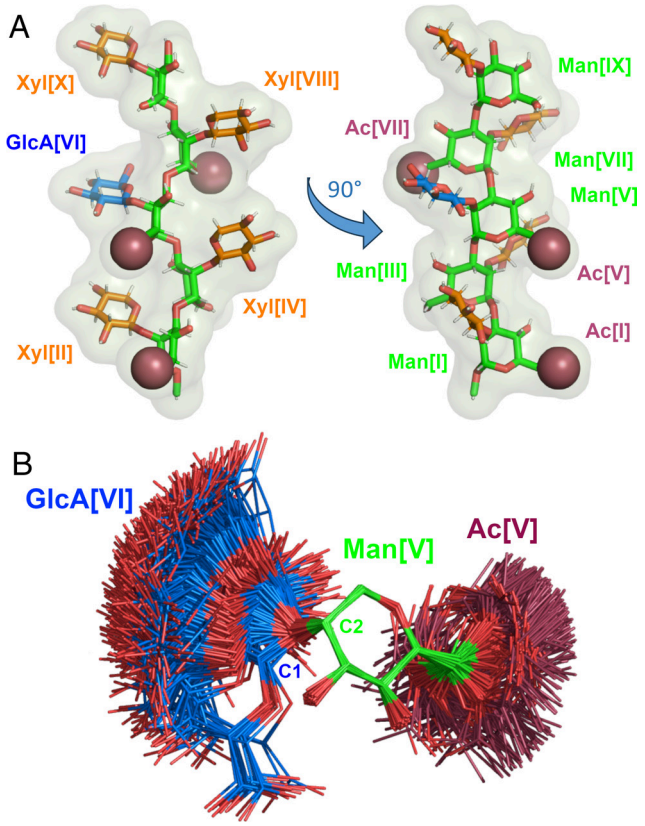

Fig. 3. GXM10-Ac$_3$ structural model. (*A*) The averaged MD structure of GXM10-Ac$_3$ (GXM10ref) is consistent with NMR-derived experimental parameters. The resulting model has an extended Man backbone with each contiguous Man ring-axis in an antiparallel orientation (green), which results in the Xyl (orange) and GlcA (blue) branches alternating sides alongside the Man backbone. The Man[I] and Man[V] *O*-acetyl groups (raspberry) align on the same side of the Man backbone while Man[VII] 6Ac and GlcA carboxyl side chain align approximately on the opposite side. (*B*) Spread of orientations of the GlcA branch relative to the Man to which is linked (500 overlayed structures from the last 500 ns MD trajectory of GXM10-Ac$_3$), showing broad freedom of movement which fluctuates between a "face-on" and "edge-on" orientation. Similar results are obtained for all branches.

GXM Polysaccharide MD Simulation. To structurally characterize the extended GXM PS, we performed a 2 μs MD simulation on an *O*-acetylated 12 M2 motif RU PS (GXM-12RU). The

GXM-12RU backbone consists of a 36 α-(1→3) linked Man chain. The previous study reported was limited to 6 RU and 500 ns (38). Standard analysis of the GXM-12RU trajectory (distance, hydrogen bonds, and torsion angles) did not reveal any pattern that could indicate the persistence of multi-residue structural features beyond what was previously described. An extension analysis of the PS over the last 500 ns showed a wide distribution of end-to-end lengths (measured from Man[1]C1 to Man[36] C1) with an average of 130.9 Å and a SD of 8.4 Å (*SI Appendix*, Fig. S10). We created Movie S4 with 10 models from the last 500 ns of the trajectory (each 50 ns apart) to further illustrate the long-scale flexibility which the PS exhibits. In the movie, each model is turned on sequentially in stick representation on top of the same 10 models, overlayed as cartoons in semitransparent gray, for easy visualization and reference. The models were fit utilizing model #5 as a reference of the entire set (arbitrarily chosen because it was the most extended with a length of ~145 Å end-to-end) to all the Man ring atoms. The resulting rmsd ranged between 5.0 and 9.4 Å, reflecting the fact that although restrained (since the molecule never collapses or contacts one end with other sections of the PS), the PS has significant freedom to contort in various shapes.

Despite the lack of an obvious structural identity, we compared the GXM trajectory to GXM10ref, described in the previous section, over the length of the PS, which for a 12 RU contains 11 such segments centered at GlcA residues, as illustrated in Fig. 4*A*. The resulting rmsd values, for each GXM segment (on 60 ring atoms) over the 2 μs trajectory, are shown in panel 4*B*. For clarity, rmsd instantaneous values were averaged over a running window of 20 ns; otherwise, the wide variation of consecutive points obscures the ability to discern any trends over the trajectory. As can be appreciated, most GXM10-Ac_3 segments start in arbitrary initial conformations not resembling that of the reference model (rmsds > 2 Å), but by approximately 1 μs, all segments have found their way to a reference model-like shape with an rmsd value of ~1.3 Å, in which they mostly remain for the duration of the simulation. This result supports the conclusion that the experimentally consistent structure GXM10ref displayed in Fig. 3*A* is uniformly present along the GXM PS.

To confirm that the results in Fig. 4*B* are not due to the arbitrary GXM-12RU initial structure (out of countless possibilities), we ran a second simulation with a minor change in the equilibration stage, reaching a maximum temperature of 323 K (instead of 310 K), before equilibrating at 300 K for production. As is normal procedure for starting MD simulations, the velocities for all atoms were randomized at the start of the simulation. These choices ensured that the new MD production stage run started from a different initial PS conformation. *SI Appendix*, Fig. S11, demonstrates that the rmsd of each decasaccharide unit in both GXM-12RU trajectories converges to the same low average value following an independent path toward equilibrium. Overall, the equivalence of these independent runs supports the argument that the general conclusions derived from the trajectory section after reaching equilibrium are valid and independent of the arbitrary starting conditions.

Next, and given the segmental persistence along the PS of a preferred shape, we investigated whether the extended PS structure could propagate into a helical pattern. To do this, we chose to define a vector originating in the backbone and ending on GlcA. Thus, we defined vectors from Man{GlcA}-C2 to GlcA-C4 for each segment and measured all dihedral angles between consecutive RUs (*SI Appendix*, Fig. S12), following their evolution throughout the trajectory (Fig. 4*C*). Utilizing a 20 ns running average reveals that the PS settles into a steady pattern after ~1.1 μs with dihedral values around 160°. A precise calculation from the representative portion

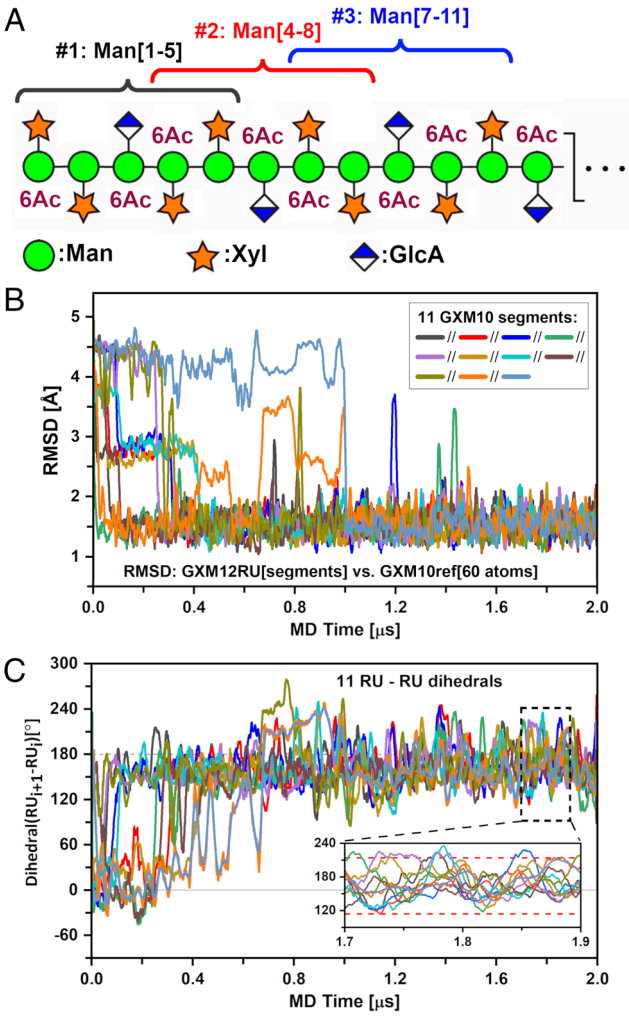

Fig. 4. GXM-12RU (M2 motif) PS MD characterization. (*A*) Scheme of GXM12-RU PS first four RUs (CFG notation), highlighting overlapping GXM10-Ac_3 units, assessed over a 2 μs MD trajectory. (*B*) rmsd of PS segments against GXM10ref. After ~1.5 μs, all segments converged to a low rmsd ~1.5 Å. (*C*) Analysis of the rotation pitch of the RUs, using dihedrals between consecutive GlcA glycans (represented by Man{C2}-GlcA{C4} vectors). Averaged values converge to ~164° ± 50° toward the end of the simulation (indicated on *Inset* with red dashed lines). In both (*B*) and (*C*) curves were smoothed using 20 ns running windows average for clarity.

shown in Fig. 4 *C*, *Inset* using instant values results in an overall dihedral distribution of 164° ± 50°. On average, the PS completes one turn every 2.2 RU (~360°/164° = 2.2). Moreover, this tendency is easily reversed based on the large SD of ±50° from instant dihedral values. Since the pitch of the helix is much larger than GXM10-Ac_3 (1.6 RU) which is the smallest oligosaccharide unit that binds strongly to many anti-GXM mAbs (24), it is unlikely that the helix is important for Ab recognition for these mAbs. However, in a recent study of synthetic GXMs, a longer oligosaccharide consisting of 2.6 RUs was shown to bind stronger than GXM10-Ac_3 for at least two mAb 3E5 isotype variants IgG_3 and IgA (41). Thus, while this structural element may not be important for all anti-GXM mAbs, the ability of the PS to form a transient helix could be important for some anti-GXM mAb recognition, and further experimental evidence is necessary to address this. Movie S4 illustrates the dynamic behavior of the PS over the last 500 ns of the MD trajectory.

We finalize this work with Fig. 5, showing three views of 6 RUs (out of 12) from the last MD trajectory frame to illustrate the GXM PS structural characteristics. This can be better described

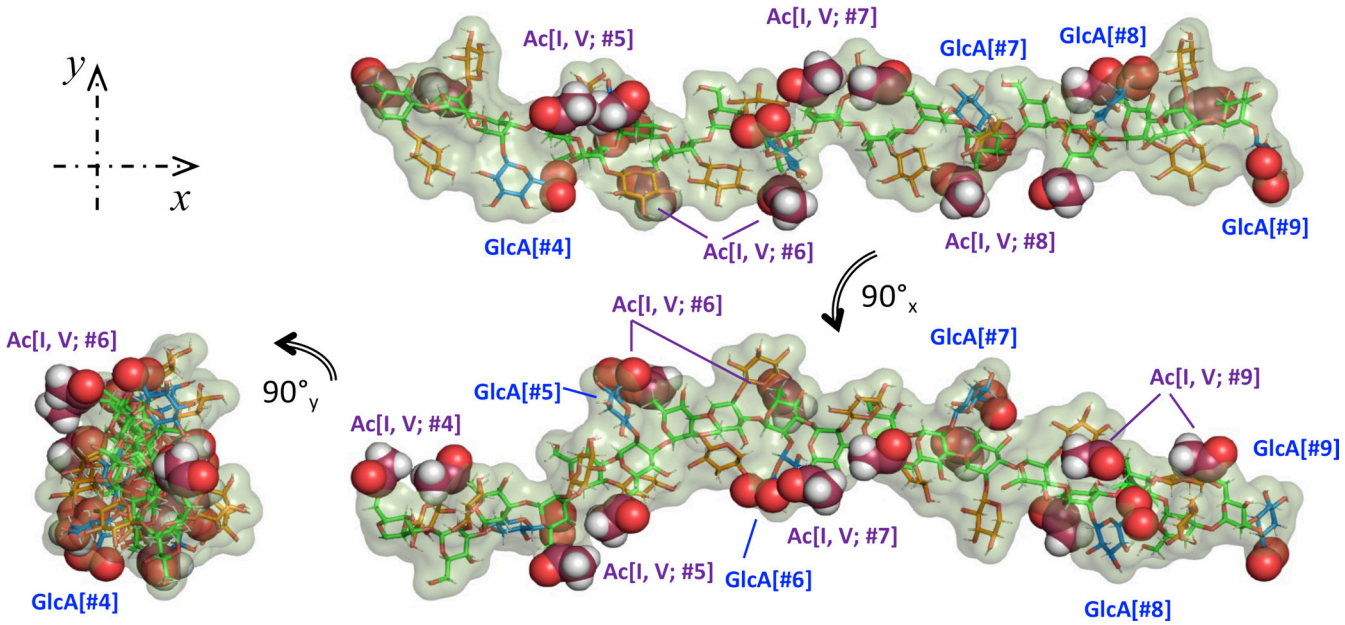

Fig. 5. Three views of 6RU (#4-#9) of the last frame of the GXM PS MD. Color scheme: green(Man{C}); red(Xyl{C}; blue(GlcA{C}; raspberry(GlcA{O6A, B}); orange(6Ac{C}). Spheres representation used for 6Ac and Glc{O6A, B} to facilitate identification.

as an extended Man backbone, with alternating orientations, and noticeable pairs of *O*-acetyl moieties, which switch sides over the length of the PS. Additionally, the GlcA carboxylic acid group in each RU appears near the 6Ac pair of the following RU. We used sphere representations to easily locate both 6Ac groups and the oxygen atoms in the carboxylic acid moieties in GlcA. The Xyl/GlcA branches, alternate sides and add volume to the chain but with considerable orientational freedom. Therefore, the PS appears to maintain steady structural features while retaining ample liberty to depart from the resulting average values. The placement of the GlcA and *O*-acetyl groups at defined intervals with alternating orientation may allow PS molecules to interact through Ca^{2+} bridges (42), creating a complex network from which the capsule emerges. Details of these structural features will be investigated in a future report.

Conclusions

Until now, a *C. neoformans* GXM PS structural characterization has remained elusive because isolated materials have been large and heterogeneous. Hence, we focused instead on characterizing the structure of an immunologically active synthetic GXM10-Ac_3 oligosaccharide utilizing modern NMR techniques combined with extended MD simulation data. Excellent agreement between NMR and MD structural analysis provides strong support for the derived representative model presented in Fig. 3*A*, allowing us to draw general conclusions as to the important features regarding Ab recognition. The alternating Man ring orientations across the backbone results in consecutive Xyl/GlcA branch locations on opposite sides of the PS. As a result, every other branched residue is close in space but with enough separation to allow ample orientational freedom. This also applies to the *O*-acetyl groups, with Man[I] and Man[V] *O*-acetyls close in space and Man[VII] *O*-acetyl on opposite sides of the Man backbone. The GXM-12RU PS MD experiments allowed us to generalize these observations to the PS, showing that the experimentally verified GXM10-Ac_3 shape is, on average, uniformly represented in the PS. In addition to maintaining this short-scale structural identity, MD also predicts that the PS forms a flexible helical pattern, with wide local pendant glycan fluctuations as well as variation in the chain length and shape. However, the predicted pitch of the helical pattern is significantly longer than GXM10-Ac_3 segments. Thus, our data suggest that the structural elements important for Ab recognition are the proximal pair of *O*-acetyl groups. Overall, the deduced GXM PS structure provides a foundation for future studies to characterize interactions between cryptococcal GXM PS and host immune factors.

Materials and Methods

Synthesis of the Decasaccharide. Synthesis of the decasaccharide was reported previously (24), which used a convergent building block approach, utilizing di-and tetrasaccharide thioglycoside building blocks (43, 44). The global deprotection was then carried out using optimized conditions (45, 46).

NMR Analysis of Synthetic Decasaccharide. All NMR experiments were performed at 700 MHz ^{1}H frequency using a Bruker Avance III HD console and 5-mm triple resonance xyz gradient cryoprobe at 20 °C. 2.5 mg of the GXM10-Ac_3were dissolved in 300 µL of a 20 mM phosphate buffer at pH* 6.4 with added DSS as an internal reference in ~99% D_2O. Two-dimensional NMR spectra were acquired using Topspin 3.6.5 software (http://www.bruker.com; Billerica, MA, USA). Data were collected with a ^{1}H spectral window of 7,002.80 Hz (10 ppm) and a ^{13}C window of 8,802.92 Hz (50 ppm) with carrier frequencies of 4.705 ppm and 83.00 ppm in ^{1}H and ^{13}C, respectively. 2,048 points were taken in ^{1}H and ^{13}C for ^{1}H-^{13}C HSQC (Bruker pulse sequence hsqcedetgp), HSQC-TOCSY (Bruker pulse sequence hsqcdietgpsi) experiments. In the LR-HSQMBC (Bruker pulse sequence hsqcetgpipjcsp2), PIP-HSQMBC (37), and NOESY (Bruker pulse sequence hsqcetf3gpno) experiments, 4,096 and 2,048 points were taken in ^{1}H and ^{13}C, respectively. ^{1}H-^{1}H NOE strength was assigned based on the NOE cross-peak SNR with a SNR ≥30:1, ≥15:1, and ≥5:1 denoted as strong, medium, and weak, respectively. The CT-cHSQC experiment (47) was taken with 50 and 17,408 points, spectral windows of 1,680.3 Hz (2.4 ppm) and 8,802.8 Hz (50 ppm), and carrier frequencies of 4.2 ppm and 83 ppm in ^{1}H and ^{13}C, respectively. Data were zero-filled to 2× the total points collected in ^{1}H and ^{13}C, and a cosine squared function was applied in both dimensions. The CT-cHSQC experiment was processed with SMILE-based linear prediction (35).

For the ^{1}H-^{13}C PIP-HSQMBC experiment, the INEPT delay was set to a 6 Hz long-range coupling constant ($1/[4J_{CH}]$ = 41.6 ms). The sum and the difference of the in-phase and anti-phase data were processed and visualized in NMRpipe (www.ibbr.umd.edu/nmrpipe, NIST). Long-range transglycosidic correlations were

identified and the peaks were fit using the NMRpipe multidimensional lineshape fitting command autoFit.tcl. To obtain the $^3J_{CH}$, the frequency difference in ^{1}H (Hz) was calculated from the sum and difference spectrum for each to yield one of the two ^{1}H-^{13}C doublet components of long-range transglycosidic *J*-correlation.

Transglycosidic Torsion Calculations. Transglycosidic $^3J_{CH}$ values obtained from the PIP-HSQMBC experiment were substituted into Zhang et al. (40) and Reeves and Wang (39) parameterized Karplus relations in order to calculate ϕ and ψ torsions. Respectively, these were

$$\text{Ser19: } {}^3J_{COCH} = 4.04 - 1.72\cos(\theta) + 0.18\sin(\theta) + 3.70\cos(2\theta) - 0.91\sin(2\theta),$$

$$\text{RW: } {}^3J_{COCH} = 6.735\cos(2\theta) - 0.58\cos(\theta) + 0.173.$$

To account for the uncertainty introduced by using these equations, the error was determined by taking the square root of experimental error squared plus the Karplus-like RMSE squared.

The above Karplus-like equations were used to obtain torsion values from experimental $^3J_{CH}$ values. The converse was also utilized, namely, we predicted $^3J_{CH}$ values from the MD trajectories. While Ser19 can be directly used for this goal, Reeves and Wang proposed a related equation in the same work to use with MD data which is the one used in the present work, that considered in addition to the torsion angle the central C-O distance (r_{CO}) from the MD simulation, expressed by the following equation:

$$\text{RW}_{MD}\text{: } {}^3J_{COCH} = (8.870\cos(2\theta) - 0.751\cos(\theta) + 0.319) \times (1 - 2.557\,(r_{CO} - 1.330)).$$

MD Simulations. MD simulations were performed using the AMBER 20 software package (48) on a workstation equipped with four GeForce GTX 1080Ti Graphic Processing Units (GPU) for oligomers up to 10 residues. For the larger oligomers (up to 12 GXM RUs), simulations were run at the FDA core facility on NVIDIA A100 GPU. All structure and parameter files for penta-Man, GXM10 w/wo Ac_3, and GXM-12RU were created using the TLEaP module included in AMBER with the force field Glycam-06j-1 (49). Following analysis of initial MD runs, it became apparent that the Xyl rings needed reinforcement to prevent intermittent puckering exchange from the normal $^4C_1$ chair to the $^1C_4$ form. This was achieved by using parabolic restraints on two torsion angles in Xyl defined to atoms [O5-C1-C2-C3] and [C3-C4-C5-O5]. Analysis was performed on these torsions to verify that the effect of restraints was limited to prevent puckering changes.

All initial conformers were solvated with TIP3FB explicit water models (50) defining cubic cells for periodic conditions with a minimum distance from the oligosaccharide to the cell border of 8 Å, except for GXM-12RU for which an octahedral cell was employed to reduce the number of water molecules needed. Na^+ counterions were used for neutralization of charges. For GXM-12RU, the cell linear dimensions were of ~170 Å containing in addition to the PS 12 sodium ions and over 79,000 waters. Nonbonded van der Waals and electrostatic scaling factors for 1 to 4 interactions were set to unity (SCEE = SCNB = 1) as required by Glycam. Long-range electrostatic interactions were computed with particle–mesh Ewald summation (51), with a nonbonded cutoff distance of 8 Å. Starting oligomer conformations with default torsion values were appropriate to proceed with energy minimization in all cases. Then, a 1 ns preparation MD run was used to equilibrate the system to the target temperature of 300 K for production, as follows: 0 to 310 K in 0.1 ns, 310 K from 0.1 to 0.6 ns, 310 to 300 K from 0.6 to 0.8 ns, and 300 K from 0.8 to 1.0 ns. MD target durations for analysis were of 2 μs at 300 K, with NPT conditions and hydrogen mass repartition (HMR) (52) to allow an integration time for the equations of motion of 4 fs, with hydrogen-containing covalent bonds constrained to their equilibrium lengths using the SHAKE algorithm (53). As mentioned in the text, for GXM10-Ac_3, the first 100 ns were regarded as equilibration based on 2D-rmsd analysis, *SI Appendix*, Fig. S6. A second independent run on GXM-12RU was done starting from the same initial structure but increasing the equilibration stage temperature from 310 to 323 K. This alone ensures different starting structure and velocities for the MD at the production stage.

Processing of trajectories was performed using *cpptraj*, included in AMBER, and python in-house scripts. General MD statistical analysis on GXM10-Ac_3 was performed over 2 μs utilizing 50,000 frames (1 every 40 ps). For distance analysis and NOE predictions we utilized the "type noe" option in *cpptraj* that reports the average distance $\langle r^{-6}\rangle^{-1/6}$. Free energy torsion maps were produced from bin populations using $G_i = -k_B T \ln(N_i/N_{Max})$, where k_B is the Boltzmann's constant, T is the MD temperature, N_i is the population of bin i, and N_{Max} is the population of the most populated bin. $^3J_{CH}$-couplings were calculated using the equations described in the previous section from instantaneous torsion values; then, standard statistics definitions were used to obtain the average and SD values for each case. Figures were created with OriginPro 2019 (www.OriginLab.com; Northampton, MA) and PyMol (https://pymol.org/2/). Movies were generated with PyMol.

Data, Materials, and Software Availability. All study data are included in the article and/or supporting information. Files necessary to reproduce MD results and trajectories used to produce the movies have been deposited to Github (54).

ACKNOWLEDGMENTS. C.J.C. was funded by an Irish Research Councill Postgraduate award (GOIPG/2016/998). S.O. is funded by SFI awards 13/IA/1959 and 20/FFP-P/884. A.C. is supported in part by NIH grants AI052733, AI152078, and HL059842. M.P.W. is supported by NIH grants AI162381 and AI152078. H.F.A. thanks Xiaocong Wang and Rob Woods for helpful advice on restraining Xyl rings in AMBER. A.A.H. thanks Jeahoo Kwon for help setting up initial NMR experiments and writing a program to aid in torsion calculations from NMR data.

Author affiliations: [a]Laboratory of Bacterial Polysaccharides, Office of Vaccines Research and Review, Center for Biologics Evaluation and Research, U.S. Food and Drug Administration, Silver Spring, MD 20993; [b]W. Harry Feinstone Department of Molecular Microbiology and Immunology, The Johns Hopkins Bloomberg School of Public Health, Baltimore, MD 21205; and [c]Centre for Synthesis and Chemical Biology, University College Dublin, Dublin 4, Ireland

Author contributions: A.A.H., H.F.A., S.O., A.C., and D.I.F. designed research; A.A.H., H.F.A., and M.P.W. performed research; C.J.C. and S.O. contributed new reagents/analytic tools; A.A.H., H.F.A., M.P.W., and D.I.F. analyzed data; and A.A.H., H.F.A., A.C., and D.I.F. wrote the paper.

1. J. A. Barnett, A history of research on yeasts 14: Medical yeasts part 2, *Cryptococcus neoformans*. *Yeast* **27**, 875–904 (2010).
2. X. Lin, J. Heitman, The biology of the *Cryptococcus neoformans* species complex. *Annu. Rev. Microbiol.* **60**, 69–105 (2006).
3. C. Coelho, A. L. Bocca, A. Casadevall, The tools for virulence of *Cryptococcus neoformans*. *Adv. Appl. Microbiol.* **87**, 1–41 (2014).
4. M. L. Rodrigues, C. S. Alviano, L. R. Travassos, Pathogenicity of *Cryptococcus neoformans*: Virulence factors and immunological mechanisms. *Microbes Infect.* **1**, 293–301 (1999).
5. S. A. Mirza *et al.*, The changing epidemiology of cryptococcosis: An update from population-based active surveillance in 2 large metropolitan areas, 1992–2000. *Clin. Infect. Dis.* **36**, 789–794 (2003).
6. R. Rajasingham *et al.*, Global burden of disease of HIV-associated cryptococcal meningitis: An updated analysis. *Lancet Infect. Dis.* **17**, 873–881 (2017).
7. R. Rajasingham *et al.*, The global burden of HIV-associated cryptococcal infection in adults in 2020: A modelling analysis. *Lancet Infect. Dis.* **22**, 1748–1755 (2022).
8. M. A. Ghannoum, L. B. Rice, Antifungal agents: Mode of action, mechanisms of resistance, and correlation of these mechanisms with bacterial resistance. *Clin. Microbiol. Rev.* **12**, 501–517 (1999).
9. A. Vecchiarelli, Immunoregulation by capsular components of *Cryptococcus neoformans*. *Med. Mycol.* **38**, 407–417 (2000).
10. F. Micoli, P. Costantino, R. Adamo, Potential targets for next generation antimicrobial glycoconjugate vaccines. *FEMS Microbiol. Rev.* **42**, 388–423 (2018).
11. A. J. Pollard, K. P. Perrett, P. C. Beverley, Maintaining protection against invasive bacteria with protein–polysaccharide conjugate vaccines. *Nat. Rev. Immunol.* **9**, 213–220 (2009).
12. R. Cherniak, H. Valafar, L. C. Morris, F. Valafar, *Cryptococcus neoformans* chemotyping by quantitative analysis of ^{1}H nuclear magnetic resonance spectra of glucuronoxylomannans with a computer-simulated artificial neural network. *Clin. Diagn. Lab. Immunol.* **5**, 146–159 (1998).
13. A. K. Bhattacharjee, J. E. Bennett, C. P. Glaudemans, Capsular polysaccharides of *Cryptococcus neoformans*. *Rev. Infect. Dis.* **6**, 619–624 (1984).
14. P. M. Ellerbroek *et al.*, *O*-acetylation of cryptococcal capsular glucuronoxylomannan is essential for interference with neutrophil migration. *J. Immunol.* **173**, 7513–7520 (2004).
15. D. C. McFadden, B. C. Fries, F. Wang, A. Casadevall, Capsule structural heterogeneity and antigenic variation in *Cryptococcus neoformans*. *Eukaryot. Cell* **6**, 1464–1473 (2007).
16. B. E. Bacon, R. Cherniak, Structure of the *O*-deacetylated glucuronoxylomannan from *Cryptococcus neoformans* serotype C as determined by 2D ^{1}H NMR spectroscopy. *Carbohydr. Res.* **276**, 365–386 (1995).
17. R. Cherniak, R. G. Jones, E. Reiss, Structure determination of *Cryptococcus neoformans* serotype A-variant glucuronoxylomannan by ^{13}C-n.m.r. spectroscopy. *Carbohydr. Res.* **172**, 113–138 (1988).
18. R. Cherniak, L. C. Morris, S. A. Meyer, Glucuronoxylomannan of *Cryptococcus neoformans* serotype C: Structural analysis by gas-liquid chromatography-mass spectrometry and ^{13}C-nuclear magnetic resonance spectroscopy. *Carbohydr. Res.* **225**, 331–337 (1992).

19. R. Cherniak, L. C. Morris, S. H. Turner, Glucuronoxylomannan of *Cryptococcus neoformans* serotype D: Structural analysis by gas-liquid chromatography-mass spectrometry and by 13C-nuclear magnetic resonance spectroscopy. *Carbohydr Res.* **223**, 263–269 (1992).
20. M. A. Skelton, H. van Halbeek, R. Cherniak, Complete assignment of the ^{1}H- and ^{13}C-n.m.r. spectra of the *O*-deacetylated glucuronoxylomannan from Cryptococcus neoformans serotype B. *Carbohydr. Res.* **221**, 259–268 (1991).
21. S. H. Turner, R. Cherniak, Glucuronoxylomannan of *Cryptococcus neoformans* serotype B: Structural analysis by gas–liquid chromatography-mass spectrometry and 13C-nuclear magnetic resonance spectroscopy. *Carbohydr. Res.* **211**, 103–116 (1991).
22. S. H. Turner, R. Cherniak, E. Reiss, K. J. Kwon-Chung, Structural variability in the glucuronoxylomannan of *Cryptococcus neoformans* serotype A isolates determined by ^{13}C NMR spectroscopy. *Carbohydr. Res.* **233**, 205–218 (1992).
23. K. J. Kwon-Chung, A. Varma, Do major species concepts support one, two or more species within *Cryptococcus neoformans*? *FEMS Yeast Res.* **6**, 574–587 (2006).
24. L. Guazzelli *et al.*, A synthetic glycan array containing *Cryptococcus neoformans* glucuronoxylomannan capsular polysaccharide fragments allows the mapping of protective epitopes. *Chem. Sci.* **11**, 9209–9217 (2020).
25. S. J. Devi *et al.*, *Cryptococcus neoformans* serotype A glucuronoxylomannan-protein conjugate vaccines: Synthesis, characterization, and immunogenicity. *Infect. Immun.* **59**, 3700–3707 (1991).
26. S. J. Devi, Preclinical efficacy of a glucuronoxylomannan-tetanus toxoid conjugate vaccine of *Cryptococcus neoformans* in a murine model. *Vaccine* **14**, 841–844 (1996).
27. A. Casadevall *et al.*, Antibodies elicited by a *Cryptococcus neoformans*-tetanus toxoid conjugate vaccine have the same specificity as those elicited in infection. *J. Infect. Dis.* **165**, 1086–1093 (1992).
28. J. Mukherjee, G. Nussbaum, M. D. Scharff, A. Casadevall, Protective and nonprotective monoclonal antibodies to *Cryptococcus neoformans* originating from one B cell. *J. Exp. Med.* **181**, 405–409 (1995).
29. C. J. Crawford *et al.*, A glycan FRET assay for detection and characterization of catalytic antibodies to the *Cryptococcus neoformans* capsule. *Proc. Natl. Acad. Sci. U.S.A.* **118**, e2016198118 (2021).
30. S. Oscarson, M. Alpe, P. Svahnberg, A. Nakouzi, A. Casadevall, Synthesis and immunological studies of glycoconjugates of *Cryptococcus neoformans* capsular glucuronoxylomannan oligosaccharide structures. *Vaccine* **23**, 3961–3972 (2005).
31. G. Bodenhausen, D. J. Ruben, Natural abundance N-15 Nmr by enhanced heteronuclear spectroscopy. *Chem. Phys. Lett.* **69**, 185–189 (1980).
32. R. T. Williamson, A. V. Buevich, G. E. Martin, T. Parella, LR-HSQMBC: A sensitive NMR technique to probe very long-range heteronuclear coupling pathways. *J. Org. Chem.* **79**, 3887–3894 (2014).
33. L. Lerner, A. Bax, Sensitivity-enhanced two-dimensional heteronuclear relayed coherence transfer Nmr-spectroscopy. *J. Magn. Reson.* **69**, 375–380 (1986).
34. L. Lerner, A. Bax, Application of new, high-sensitivity, ^{1}H–^{13}C-n.m.r.-spectral techniques to the study of oligosaccharides. *Carbohydr. Res.* **166**, 35–46 (1987).
35. J. Ying, F. Delaglio, D. A. Torchia, A. Bax, Sparse multidimensional iterative lineshape-enhanced (SMILE) reconstruction of both non-uniformly sampled and conventional NMR data. *J. Biomol. NMR* **68**, 101–118 (2017).
36. F. A. L. Anet, A. J. R. Bourn, Nuclear magnetic resonance spectral assignments from nuclear overhauser effects. *J. Am. Chem. Soc.* **87**, 5250–000 (1965).
37. L. Castanar, J. Sauri, R. T. Williamson, A. Virgili, T. Parella, Pure in-phase heteronuclear correlation NMR experiments. *Angew. Chem. Int. Ed. Engl.* **53**, 8379–8382 (2014).
38. M. M. Kuttel, A. Casadevall, S. Oscarson, *Cryptococcus neoformans* capsular GXM Conformation and epitope presentation: A molecular modelling study. *Molecules* **25**, 2651 (2020).
39. H. L. Reeves, L. P. Wang, The impact of conformational sampling on first-principles calculations of vicinal COCH *J*-couplings in carbohydrates. *Glycobiology* **33**, 38–46 (2023).
40. W. Zhang *et al.*, Use of circular statistics to model alphaMan-(1–>2)-alphaMan and alphaMan-(1–>3)-alpha/betaMan o-glycosidic linkage conformation in (13)C-labeled disaccharides and high-mannose oligosaccharides. *Biochemistry* **58**, 546–560 (2019).
41. C. J. Crawford *et al.*, Synthetic glycans reveal determinants of antibody functional efficacy against a fungal pathogen. *ACS Infect. Dis.*, 10.1021/acsinfecdis.3c00447 (2023).
42. L. Nimrichter *et al.*, Self-aggregation of *Cryptococcus neoformans* capsular glucuronoxylomannan is dependent on divalent cations. *Eukaryot. Cell* **6**, 1400–1410 (2007).
43. L. Guazzelli, R. Ulc, S. Oscarson, Synthesis of benzyl protected beta-D-GlcA-(1–>2)-alpha-d-Man thioglycoside building blocks for construction of *Cryptococcus neoformans* capsular polysaccharide structures. *Carbohydr. Res.* **389**, 57–65 (2014).
44. L. Guazzelli, R. Ulc, L. Rydner, S. Oscarson, A synthetic strategy to xylose-containing thioglycoside tri- and tetrasaccharide building blocks corresponding to *Cryptococcus neoformans* capsular polysaccharide structures. *Org Biomol. Chem.* **13**, 6598–6610 (2015).
45. C. Crawford, S. Oscarson, Optimized conditions for the palladium-catalyzed hydrogenolysis of benzyl and naphthylmethyl ethers: Preventing saturation of aromatic protecting groups. *Eur. J. Org Chem.* **2020**, 3332–3337 (2020).
46. C. J. Crawford *et al.*, Defining the qualities of high-quality palladium on carbon catalysts for hydrogenolysis. *Org. Process Res. Dev.* **25**, 1573–1578 (2021).
47. M. D. Battistel, D. I. Freedberg, Dispersing the crowd: Adopting (13)C direct detection for glycans. *J. Magn. Reson.* **318**, 106792 (2020).
48. D. A. Case *et al.*, *AMBER 2015* (University of California, San Francisco, 2015).
49. K. N. Kirschner *et al.*, GLYCAM06: A generalizable biomolecular force field. Carbohydrates. *J. Comput. Chem.* **29**, 622–655 (2008).
50. L. P. Wang, T. J. Martinez, V. S. Pande, Building force fields: An automatic, systematic, and reproducible approach. *J. Phys. Chem. Lett.* **5**, 1885–1891 (2014).
51. D. M. York, T. A. Darden, L. G. Pedersen, The effect of long-range electrostatic interactions in simulations of macromolecular crystals–A comparison of the ewald and truncated list methods. *J. Chem. Phys.* **99**, 8345–8348 (1993).
52. C. W. Hopkins, S. Le Grand, R. C. Walker, A. E. Roitberg, Long-time-step molecular dynamics through hydrogen mass repartitioning. *J. Chem. Theory Comput.* **11**, 1864–1874 (2015).
53. W. F. Vangunsteren, H. J. C. Berendsen, Algorithms for macromolecular dynamics and constraint dynamics. *Mol. Phys.* **34**, 1311–1327 (1977).
54. A. A. Hargett *et al.*, FDA/MD-of-Glycans. Github. https://github.com/FDA/MD-of-Glycans. Deposited 25 January 2024.